Hunting Planets and Observing Disks with the JWST NIRCam Coronagraph

John E. Krist[a], Charles A. Beichman[a], John T. Trauger[a], Marcia J. Rieke[b], Steve Somerstein[c], Joseph J. Green[a], Scott D. Horner[c], John A. Stansberry[b], Fang Shi[a], Michael R. Meyer[b], Karl R. Stapelfeldt[a], Thomas L. Roellig[c]
[a]NASA Jet Propulsion Laboratory, 4800 Oak Grove Dr., Pasadena, CA 91109; [b]University of Arizona/Steward Observatory, Tucson, AZ 85721; [c]Lockheed-Martin Advanced Technology Center, 3170 Porter Dr., Palo Alto, CA 94304; [d]NASA Ames Research Center, Moffett Field, CA 94035

ABSTRACT

The expected stable point spread function, wide field of view, and sensitivity of the NIRCam instrument on the James Webb Space Telescope (JWST) will allow a simple, classical Lyot coronagraph to detect warm Jovian-mass companions orbiting young stars within 150 pc as well as cool Jupiters around the nearest low-mass stars. The coronagraph can also be used to study protostellar and debris disks. At $\lambda = 4.5$ μm, where young planets are particularly bright relative to their stars, and at separations beyond ~0.5 arcseconds, the low space background gives JWST significant advantages over ground-based telescopes equipped with adaptive optics. We discuss the scientific capabilities of the NIRCam coronagraph, describe the technical features of the instrument, and present end-to-end simulations of coronagraphic observations of planets and circumstellar disks.

Keywords: James Webb Space Telescope, NIRCam, coronagraph, extrasolar planets, circumstellar disks

1. INTRODUCTION

The search for extrasolar planets is one of the leading topics in current astronomical research. The increasing number of planets detected by radial velocity measurements, transits, and microlensing events shows that solar systems beyond our own, though perhaps not necessarily like our own, are commonplace. However, these techniques have limitations: radial velocity measurements are sensitive to planets closer than a few AU to inactive stars in non-pole-on orientations, transits are only sensitive to edge-on systems, and microlensing events are serendipitous and non-repeating. These detection techniques are indirect and do not produce images of the planets. An undisputed image of an extrasolar planet has yet to be obtained. Direct imaging provides important characteristics of planets that cannot be measured using the aforementioned techniques, such as general spectral properties, complete orbital parameters, temperature, surface gravity, composition, and masses. Direct imaging can also be used to detect planets at larger distances from the stars than the radial velocity techniques.

The difficulty in imaging extrasolar planets lies in the fact that the brightness difference between even a giant planet and its star is great. Jupiter, for instance, would appear 10^9 times fainter in reflected light than the Sun when viewed from another star. When observed with a telescope, the planet would be lost underneath the star's diffracted and scattered light. Even with a coronagraph to suppress the diffraction pattern, the scattered starlight would still overwhelm the planet. Wavefront control using deformable mirrors has only recently achieved the level of scattered light suppression necessary to see planets with contrasts of 10^{-9} relative to the star[1].

The situation greatly improves at infrared wavelengths, where the ratio of the planet's thermal emission to the stellar flux is much higher than its reflected light ratio, especially for young, warm, giant planets (Figure 1). At $\lambda = 4.5$ μm, where there is a predicted peak in emission (Figure 2), the contrast of a 1 Gyr-old Jupiter is 10^{-6}, and at 100 Myr it is 10^{-4}. More massive planets would have even more favorable contrasts. These levels would be achievable with the most advanced ground-based coronagraphs on large telescopes were it not for the thermal emissions from the atmosphere and telescope that create a significant background at this wavelength. The solution is to observe from space using a cool telescope, free from atmospheric turbulence and emission.

The James Webb Space Telescope (JWST) is a 6.5 m diameter segmented telescope optimized for observations in the near-to-mid infrared (λ = 1 – 30 μm). Three cameras, all containing coronagraphs, will provide imaging across this wavelength range. The Near-Infrared Camera (NIRCam) discussed here covers the range λ = 0.7 – 5.0 μm. JWST is currently under construction and is scheduled for launch in 2013.

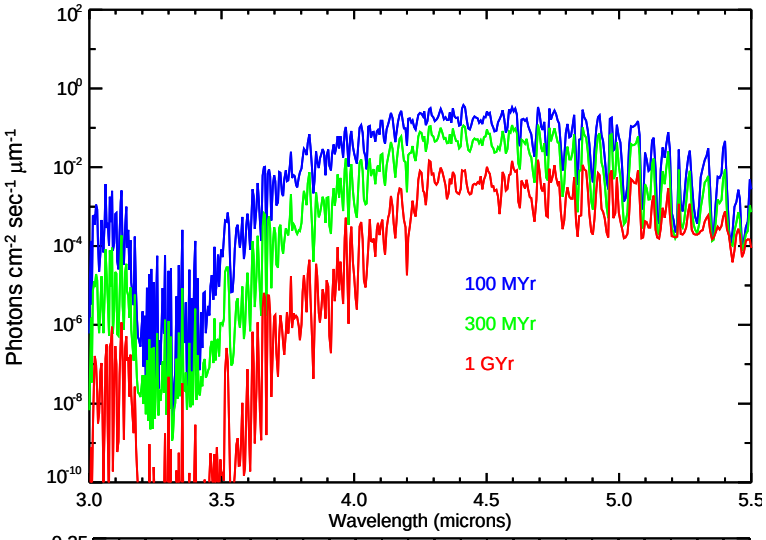

Figure 1. Model spectra[2] of a 2 Jupiter-mass planets of various ages. On this plot, a stellar spectrum would be slowly decreasing in flux with increasing wavelength.

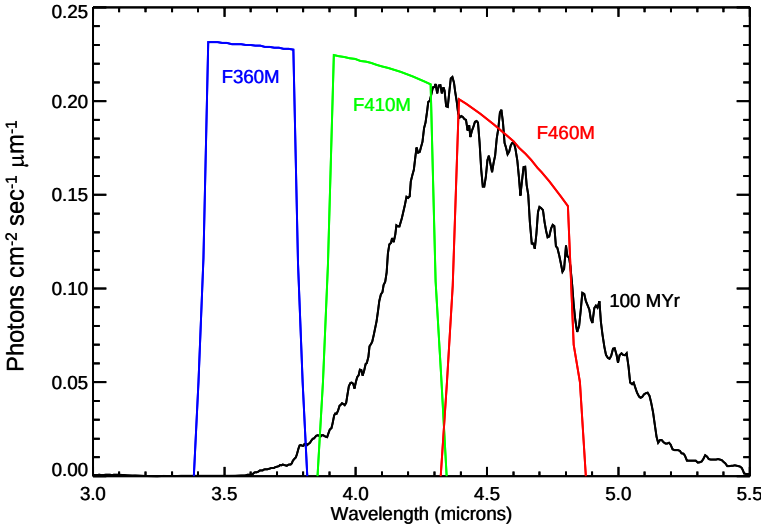

Figure 2. Model spectrum[2] of a 100 Myr old, 2 M_{Jup} planet with selected NIRCam filter passbands overplotted. The spectrum of a star would be nearly flat over this wavelength range.

2. HIGH CONTRAST IMAGING WITH JWST

JWST is designed for conventional imaging and spectroscopy, and it has no requirements tailored to high-contrast observations. Its segmented primary mirror produces a complex diffraction point spread function (PSF) with considerable flux in the wings. While a coronagraph can be used to reduce the level of the diffracted light, the complexity of the JWST aperture makes suppression difficult without a significant reduction in throughput. In addition, uncorrectable optical surface errors scatter light into the PSF wings that cannot be reduced using a coronagraph. The telescope has a wavefront error budget[3] (over all spatial frequencies) prior to the instruments of 131 nm RMS (1/15 wave @ λ=2 μm) after optimization of the primary mirror figure by actuators on the segments.

As is the case with the Hubble Space Telescope, to achieve the best possible contrast, the scattered and residual diffracted light must be removed using PSF subtraction. An image of another star, or the same star observed at a different orientation of the telescope, is subtracted from the target image. The success of this technique critically depends on having a constant PSF (and thus wavefront) between the science and reference star observations. The wavefront can differ due to thermal variations caused by changes in the attitude of the telescope relative to the Sun or by flexure caused

by motion of the telescope during slews. The JWST wavefront stability requirement[3] of 54 nm RMS (excluding NIRCam) is sufficient to maintain the shape of the PSF core, but it is lax enough to limit the effectiveness of PSF subtraction. Relative to a telescope on the ground, however, JWST should be incredibly stable.

Despite the lack of any requirements to optimize its high contrast imaging performance JWST, by virtue of being free of atmospheric turbulence and thermal background, will provide an unmatched platform for thermal IR observations.

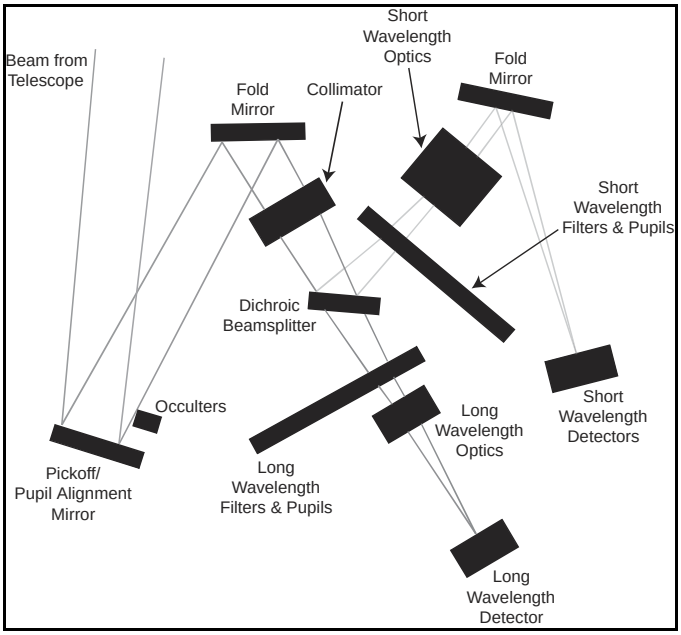

Figure 3. Schematic layout of a NIRCam imaging module.

3. OVERVIEW OF THE NEAR-INFRARED CAMERA (NIRCAM)

NIRCam comprises two redundant modules, each containing short (λ = 0.7 – 2.3 μm) and long (λ = 2.4 – 5.0 μm) wavelength channels (Figure 3). The two channels in each module view the same field using a dichroic beam splitter. Each channel has two filter wheels located at a pupil plane that contain a variety of wide-to-narrow bandpass filters, pupil imaging lenses and masks for wavefront sensing, and coronagraphic Lyot stops. An actuated pickoff mirror at the NIRCam entrance provides proper alignment of the pupil image, compensating for any transverse mechanical misalignment between the camera and telescope. Refractive optics in each channel are used to collimate the beam and to refocus it onto the detector.

The detectors are Teledyne/Rockwell Scientific Hawaii-2RG HgCdTe 2048×2048 arrays with 18 μm pixels. In the short wavelength channel, they are arranged in a 2 by 2 mosaic covering a 2.2' by 2.2' field in each module with 0.032 arcsec/pixel. In the long wavelength channel, a single detector covers the same field size at 0.065 arcsec/pixel.

4. THE NIRCAM CORONAGRAPH

4.1 Coronagraph performance goals

Each NIRCam module will be equipped with a simple Lyot coronagraph consisting of a selection of focal plane occulters and pupil masks (Lyot stops). Because there are no JWST high contrast performance requirements, there are also no formal requirements on the coronagraph. It is considered to be a relatively low-risk, low-cost addition to the camera, and it must accept whatever image the telescope produces. Given these limitations, a set of desired features and informal performance goals were defined by the NIRCam Science Team that guided the design of the coronagraph:

1. Provide imaging to within 0.6" (4λ/D) of the star at λ = 4.6 μm and to within 0.3" at λ = 2.1 μm for the detection of extrasolar planets seen in emission. The 0.6" radius corresponds to the maximum apparent separation of Jupiter if it were observed around a star 8.3 pc distant. To maintain coronagraphic performance, the occulter must vary in width to match the PSF size at any wavelength.

2. Provide imaging to within 0.8" (6λ/D) of the star at λ = 4.3 μm, 0.64" at λ = 3.35 μm, and 0.4" at λ = 2.1 μm for observations of circumstellar disks seen in reflected light. The 0.8" radius corresponds to a separation of 40 AU around a star 50 pc distant. A radially-symmetric occulter is used to provide uninterrupted imaging at all azimuths around the star.
3. The occulters must be rigidly mounted and must not interfere with imaging during non-coronagraphic observations, requiring placement outside the normal field of view.
4. Ideally, suppress the diffraction pattern produced by the JWST obscurations to a level equal to or below the scattered light created by the uncorrectable optical surface errors, given the budgeted ~131 nm RMS of wavefront error prior to the coronagraphic occulters.
5. Provide sufficient throughput to image 1 Gyr-old Jupiter-mass planets around the nearest late-type stars with 1-2 hours of exposure time.
6. Tolerate 2% pupil misalignments due to pupil wheel positioning errors and telescope-to-instrument rotational offsets.
7. Tolerate 10-40 milliarcseconds of pointing error at λ = 4.6 μm without a significant decrease in performance.

4.2 Coronagraph design

In recent years, a wide variety of schemes besides classical Lyot coronagraphs have been developed to suppress diffraction for high contrast imaging, including amplitude or phase apodization of the pupil, shaped pupils, and interferometric nulling. Some of these have limitations that make them poorly suited to the complex JWST pupil, are too sensitive to the expected pointing or pupil alignment errors, or are unacceptably expensive and complex to implement. The Lyot coronagraph is relatively simple and its performance is well understood, making it the preferred option for NIRCam. It uses an occulter placed at the focal plane of the telescope that blocks the central portion of the PSF. This has the effect of spatially filtering the pupil and concentrating the remaining light around the diffracting edges. After the occulter, an image of the pupil is formed. The bright regions are masked by the Lyot stop, which has holes to allow light through from off-axis, unocculted sources. The Lyot stop pattern must be matched to a specific occulter, and there are tradeoffs between throughput, occulter size, and sensitivity to errors. After the Lyot stop, the image is reformed at the detector with the diffraction pattern greatly suppressed.

4.3 Coronagraph occulters

The simplest occulters are dark, hard-edged spots, but their diffraction control performance is poor. Better results are achieved with grayscale (or pseudo-grayscale) occulters with transmission patterns chosen to optimize suppression when used with an appropriate Lyot stop. These patterns can range from simple Gaussians to more elaborate "band-limited" profiles[4]. Phase masks can also be used in the image plane with similar effects, and the JWST MIRI coronagraph, which operates at λ = 5 – 27 μm, includes some[5]. Their expected reduced performance at shorter wavelengths on JWST and over broad bandpasses makes them unsuitable for NIRCam.

The NIRCam Science Team has chosen to use grayscale occulters due to their ease of manufacture and performance. A variety of patterns were evaluated[6], including ones matched to the asterisk-shaped core of the JWST PSF. Attempts were also made to design optimized band-limited occulters. Most of these failed to meet the previously listed performance goals, either due to high sensitivity to pointing/alignment errors or poor throughput after the Lyot stop. Two patterns were eventually selected: sinc-squared profile wedges and sombrero-squared (Bessell) profile circular spots (Figure 4). These have the following transmission profiles for a given width, σ, and radius from the center, *r*:

$$T_{\mathrm{somb}^2}(r) = \left[1 - \left(\frac{2J_1(\sigma r)}{\sigma r}\right)^2\right]^2 \qquad T_{\mathrm{sinc}^2}(r) = \left[1 - \left(\frac{\sin(\sigma r)}{\sigma r}\right)^2\right]^2$$

The linear, wedge-shaped sinc^2 occulter varies in width to allow consistent performance over a wide range of wavelengths. The matching Lyot stop has been optimized for a 4λ/D half-width-half-maximum (HWHM) intensity transmission occulter. For a given wavelength, the star can be positioned at the wedge location corresponding to this width. There are separate wedges for short and long wavelength observations, varying over HWHM = 2λ/D - 6λ/D at λ

= 2.1 μm and 4.6 μm. The occulters are 20" long and are aligned to block the image of the diffraction spike generated by a secondary mirror support strut. Because they offer the closest imaging to the star and can be tuned for the observation wavelength, the wedge occulters are favored for detecting extrasolar planets. To prevent it from interfering with non-coronagraphic observations, the substrate containing the occulters is located just outside the normal field of view, and a telescope pointing offset places the star on the occulter. To redirect the beam onto the detector, a wedge prism is placed just behind the Lyot stop.

There are three sombrero-squared circular occulters that correspond to HWHM = 6λ/D at λ = 2.1, 3.35, and 4.3 μm (0.4", 0.64", and 0.8", respectively). While their diffraction suppression performance is less than the wedges, they and their matching Lyot stop generate a more uniform background in the final image. This and their uninterrupted 360º fields around the star make them the best choice for imaging extended sources such as circumstellar disks.

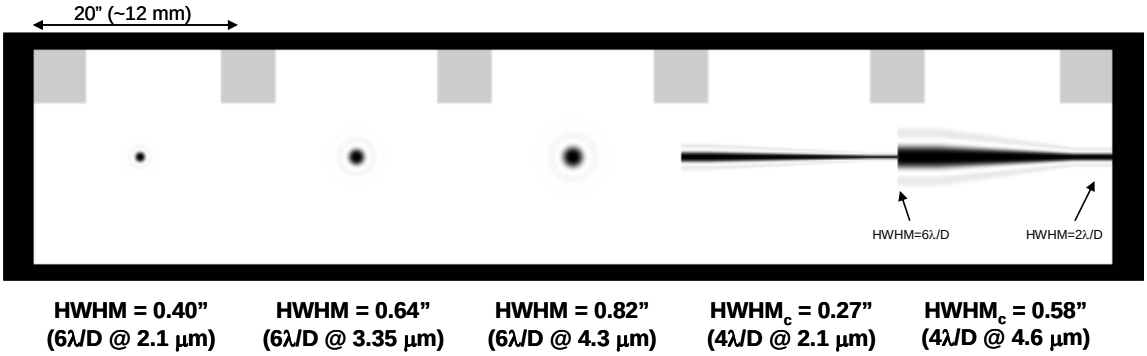

Figure 4. Layout of the coronagraphic occulters on the mounting substrate. Along the top are 5" by 5" neutral density squares used for target acquisition. The wedges for the short (thin) and long (thick) wavelengths are on the right.

The occulters will be halftone patterns composed of 0.8 μm diameter aluminum or gold dots created using vapor deposition and photo-etching on a sapphire substrate, which measures 60 mm by 12 mm (100 arcsec by 20 arcsec). Deposited gold neutral density (OD=3, or 10^{-3} transmission) squares, 5" on a side, are aligned along the top of the substrate and will be used for target acquisition.

Optical modeling has been used compute tolerances for the occulters. The minimum transmission must be 10^{-4} or less to keep the contrast within a factor of two of a perfect occulter. While the profiles are theoretically infinite in extent, it appears that only the core and first sidelobe of the sinc^2 profile need to be kept, and just the core of the sombero^2 profile is necessary. In a system with a simpler diffraction pattern, there would be greater sensitivities to the profiles.

4.4 Coronagraph Lyot stops

The Lyot stop patterns are specifically matched to the light distribution in the reimaged pupil planes after the occulters. Figure 5 shows the computed pupil intensity distributions for sources occulted by the 4λ/D wedge and 6λ/D spot (the pattern is the same regardless of wavelength for perfect optics as long as the occulter size scales with wavelength). The pupil image created by an unocculted source would have uniform intensity. The dark zones are created by the effective filtering of low spatial frequency components in the entrance pupil by the occulter. By masking the bright zones, corresponding to the higher spatial frequencies (the wings of the PSF), most of the light in the diffraction pattern can be removed. Holes in the mask matching the dark zones (Figure 6) allow light from an unocculted source to pass, though at a reduced intensity.

Using the computed pupil images, for each occulter pattern the holes in its corresponding Lyot stop were defined by the dark zones' isophotal contours. The contour levels were chosen to create a stop that would tolerate a 2% pupil misalignment and have a total mask transmission of no less than ~20% (in actuality, it is ~19% for each). The zones created by the wedge have fairly straight sides, which are efficiently approximated by polygonal holes, while a spot occulter creates rounded dark zones.

Due to the complexity of the JWST PSF, the coronagraph cannot fully suppress the diffraction pattern (i.e. the occulters are not fully band-limited). A small fraction of light leaks into the dark zones and is diffracted by the Lyot stop, creating

low-intensity residual patterns in the final image. With the wedge occulters, a broad spike appears perpendicular to the wedge long axis. Using the spot occulters, the residual light is more uniformly distributed in azimuth around the star by the rounded holes. The occulters also do nothing to suppress the mid-spatial-frequency optical errors in the telescope, which scatter light within the dark zones of the pupil (Figure 5).

The Lyot stops define the PSF of unocculted field sources in coronagraphic images. Compared to non-coronagraphic imaging, the aggressive masking of the pupil redistributes a significant fraction of light from the core into the wings. At $\lambda = 4.6$ μm, for instance, the non-coronagraphic PSF has 68% of its total flux within the first Airy ring, while the PSF created by either Lyot stop has only 16% within the same area (not including the 81% reduction in total intensity due to the stop transmission).

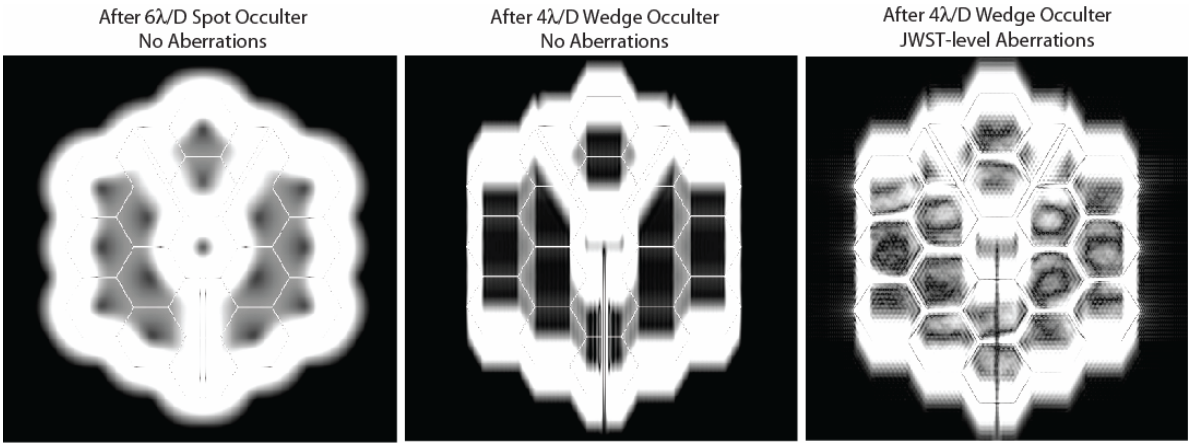

Figure 5. Computed pupil intensity patterns viewed in the Lyot stop plane for a point source occulted by the 6λ/D circular spot (left) and the 4λ/D wedge (middle) without aberrations. On the right is the pattern including JWST-level wavefront aberrations (the fine grid structure is print-through from the primary mirror backplane). The images have been displayed to emphasize the low-level features. The bright regions will be masked by the Lyot stops.

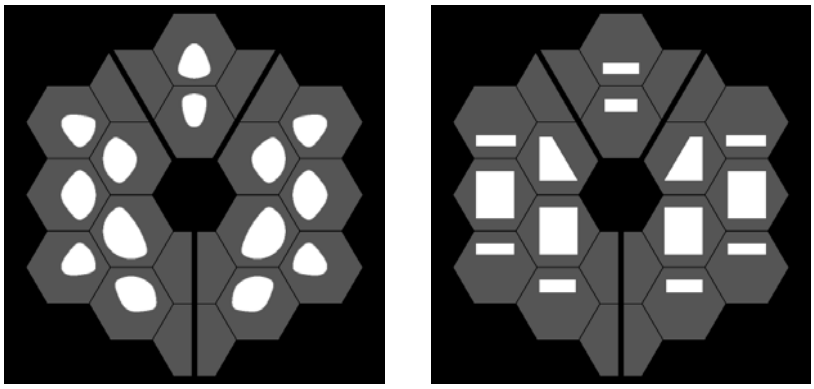

Figure 6. Openings in the Lyot stops (white) superposed on the JWST pupil pattern. The throughput for each is ~19%.

Each Lyot stop is placed on top of a wedge prism that redirects the beam onto the detector. There are two methods under consideration for constructing the stops: depositing gold or aluminum coatings directly on the prisms or cutting masks out of thin metal plates that are placed just in front of the prisms. The short wavelength prisms are made of BaF_2 and the long of silicon. BaF_2 was chosen to minimize chromatic dispersion at the shorter wavelengths, though it does not eliminate it (the core of the PSF is elongated along the dispersion direction by a factor of ~2 over a 10% bandpass at $\lambda_c =$

2 μm). While the stops have been defined for a perfect system, the actual image of the pupil at the stop is distorted due to the collimator optics, so the openings must be distorted as well to match. Because the Lyot stop shares the same wheel as the narrowband filters, narrowband coronagraphic imaging is not possible.

5. CORONAGRAPH OPERATION

5.1 Target acquisition

The performance of the coronagraph is dependent on the location of the point source behind the occulter. If the source is offset from the occulter center, the amount of residual diffracted light will increase and its pattern will change. The expected absolute pointing accuracy of JWST is unlikely to be better than 1", if only because star catalog positions are not better known. The target must be centered behind the occulter more accurately than that, so its position must be measured directly from an image taken with the camera. A target acquisition will be performed prior to a sequence of coronagraphic observations. The majority of sources will be bright stars that would otherwise saturate the detector if observed in the shortest exposure and narrowest available filter, so the target will first be placed in the neutral density square nearest to the occulter. The on-board computer will automatically measure the center of the target to subpixel accuracy and compute the offset required to center it behind the requested occulter. The estimated pointing error over this distance is <20 mas. In order to image the ND squares on the detector, the Lyot stop with its wedge prism must be in the beam during acquisition. The combination of the Lyot stop and ND square reduces the peak pixel intensity by a factor of ~22500 at $\lambda = 4.6$ μm.

5.2 Coronagraphic observations

Excluding that an occulter and Lyot stop are used and a target acquisition must be performed, a coronagraphic observation will be no different from a standard NIRCam exposure. The total integrated exposure time on a typical target will probably be 1 – 2 hours in order to detect a planet or disk and longer to characterize it using multiple filters. The images will be calibrated in the standard way (flat fielding, etc.), but because the Lyot stop alters the vignetting, flat fields specific to the coronagraph must be used. Also, the transmission response of the occulter must be divided out.

5.3 Post-processing residual light subtraction

As previously noted, the NIRCam coronagraphs cannot completely remove the PSF of the central source. A halo of scattered and partially-suppressed diffracted light will remain containing streaks, rays, spikes, and a host of other features. Without any additional processing, it would be difficult to detect faint nearby sources in such data. However, due to the expected stability of the optical system, it will be possible to subtract the image of a reference PSF from the data to remove most of the remaining light. The reference PSF may be an image of another star or the image of the same star observed at a different roll orientation of the telescope.

Roll subtraction is the best choice for planet detection as it avoids color mismatches between the target and reference PSFs that could lead to significant residuals. Exposures are taken at one orientation of the telescope, which is then rotated about the target, and another identical image set is obtained. Image features produced by the telescope and camera (i.e. the PSF) will appear to remain fixed on the detector while the image of the sky (including any planets) will appear to rotate. Subtraction of the two will then produce positive and negative images of the planet separated by the roll angle of the telescope. More sophisticated algorithms can be applied using multiple roll angles to solve for the static and dynamic portions of the image. The primary limitation of this method on JWST is the maximum allowed rotation of 10º during any given observing window (in comparison, HST can do 30º). This means that at $4\lambda/D$ from the star, a planet would appear to have moved a little more than half of its Airy disk diameter, making separation of the images at the two rolls more difficult.

Roll subtraction is not optimal for imaging extended features such as circumstellar disks because the disk at one roll angle may subtract a significant portion of itself at the other. In this case it is best to use an image of another star assumed to be free of nearby sources. Care must be taken that the two sources are very similar in color in the filters used in order to avoid PSF mismatches. It will also be important to schedule the target and reference PSF observations close together in time to avoid temporal wavefront variations.

The temporal wavefront stability of JWST is the greatest unknown in estimating the ultimate contrast level achievable with the coronagraph because it affects how well the PSF can be subtracted. The wavefront error budget allows up to 54 nm RMS of change over any timescale. Thermal models have yet to be run to estimate the wavefront changes due to

rolling the telescope between observation sequences of the same target or between back-to-back observations of the target and reference PSF star. Thus, it is necessary to assume a range of wavefront changes when estimating the coronagraphic performance after PSF subtraction.

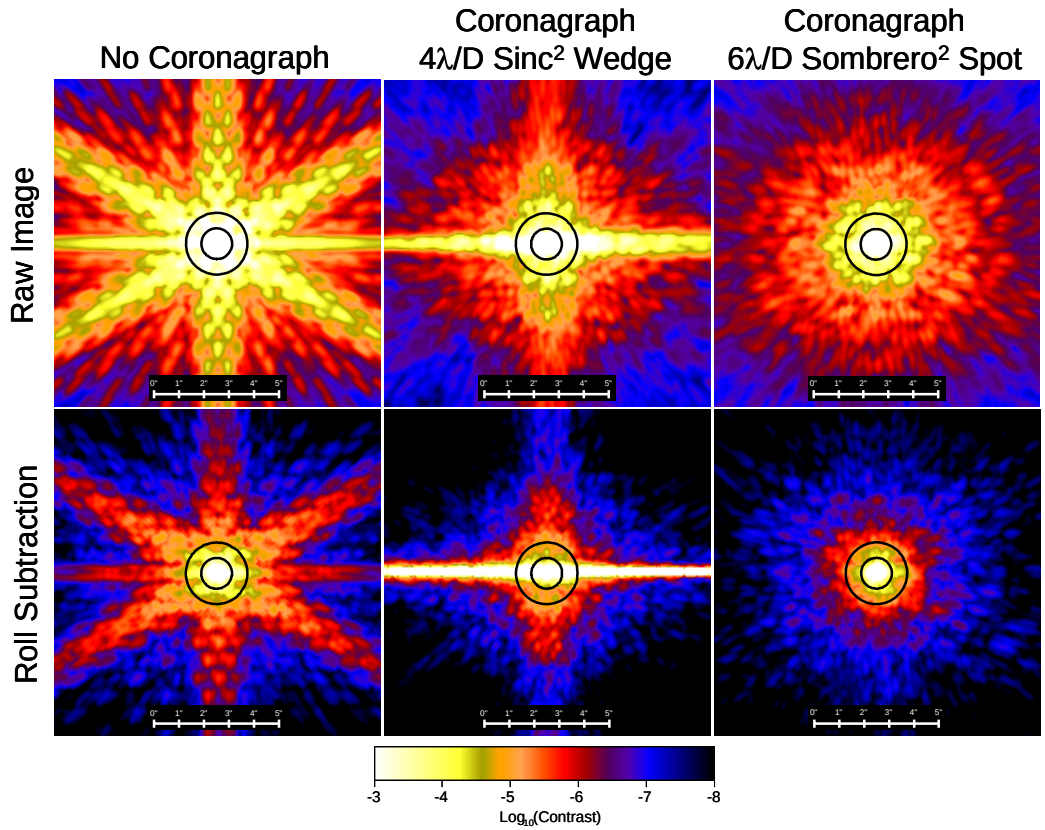

Figure 7. Contrast maps for filter F460M (λ_c = 4.6 μm) for direct (non-coronagraphic) and coronagraphic observations. On the bottom are the maps for the roll subtractions, which are simulated by subtracting two images that differ in wavefront error by 40 nm RMS (on the high side of the desired stability levels). Contrast is defined here to be the total flux of a field point source relative to the total stellar flux when the core of the point source has the same amount of flux as a similar area of the background. The circles at the centers of the images have radii of 0.58" and 1.17" (4λ/D and 8λ/D).

6. NIRCAM CORONAGRAPH PERFORMANCE

6.1 Simulations

To evaluate the performance of the NIRCam coronagraph, images were computed using the PROPER optical modeling library for IDL[7] with additional code to include certain JWST-specific characteristics (e.g. print-through from the backplane grid on the primary mirror segments and secondary mirror). The software can compute the diffraction and propagation of a wavefront through a series of optical elements, including occulters, masks, and aberrated surfaces. For the NIRCam simulations, a simplified system was used. Although the software can propagate the wavefront between any number of optical elements, in this case the primary was the only surface prior to the occulter – the aberrations in the intervening optics were added to those in the primary (at the contrast levels of interest, this produces sufficiently accurate results). The levels of low, mid, and high-spatial-frequency aberrations were set to match the JWST wavefront error budget as closely as possible. The entrance pupil included the segmented JWST aperture pattern and the support struts for the secondary mirror. Each segment had random, low-order aberrations defined by Zernike polynomials, up to Z_{11} (spherical) to represent figuring errors. Focus, tip-tilt, and piston were down-weighted as they are largely correctable by the segment actuators. Finer-scale figuring errors were added over the pupil by creating an aberration map defined by

a power spectral density (PSD) curve. Finally, the mirror backplane grid print-through errors in the primary and secondary were added.

The aberrated wavefront was propagated from the primary to the occulter, with the PSF sampling set to be 20% better than Nyquist. It was then propagated to the subsequent pupil (Lyot) plane where camera-specific aberrations were added and the Lyot stop mask applied. The wavefront was then propagated to the final image plane where it was integrated onto detector-sized pixels. To create a polychromatic image for a particular passband, monochromatic models were generated at multiple wavelengths and added together with weights defined by the object spectrum and system throughput. When simulating the impact of temporal variations on PSF subtractions, random low-order aberrations were added to the static wavefront.

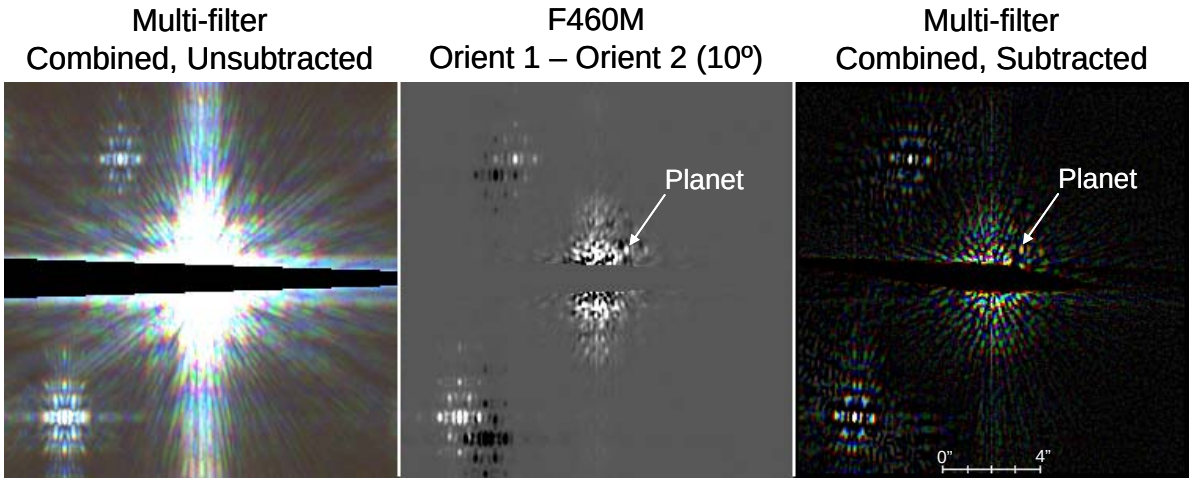

Figure 8. Simulated observations of a 1 Gyr-old, M0V star at 4 pc with the NIRCam coronagraph (wedge occulter). Exposures of 5000 sec each in filters F360M, F410M, and F460M were taken at two orientations of the telescope separated by 10º. A 2 M_J planet is shown at an apparent separation of 7 AU. Two field stars are also included: G2V (V=17.4) and M2V (V=18.0). (LEFT) Multicolor (F360M=blue, F410M=green, F460M=red) unsubtracted observations at the first orientation; (MIDDLE) Subtraction of F460M image taken at the second orientation from the first; (RIGHT) Multicolor subtracted images. The planet appears red because most of the flux is in the F460M filter. The subtractions at each filter were obtained using an iterative procedure that solves for the common rotating objects (field stars & planet) and static objects (residual light pattern from the occulted star). This combined image has been mildly unsharp masked to improve contrast. All of the images have the same static JWST wavefront aberrations plus random 5 nm RMS errors to represent exposure-to-exposure instabilities. In addition, the images at the second roll have an additional 20 nm RMS to represent orientation-induced changes to the wavefront.

6.2 Predicted contrast performance

The coronagraph significantly suppresses the wings of the occulted star's PSF (after accounting for the 81% reduction in throughput due to the Lyot stop). Unfortunately, some of this reduction is lost because the multiple apertures in the Lyot stop redistribute some flux from the core of a field PSF (e.g. a planet) into its wings. The simulations show that at λ = 4.6 μm with the wedge occulter the coronagraph reduces the median surface brightness of the PSF wings by factors of 10 – 25 over a radius of 0.6" – 5". However, the field PSF has 5.8 times less flux in its peak than it has without the coronagraph, so the net effective improvement is a factor of 1.7 – 4.3. Figure 7 shows contrast maps for the case where the detection limit is defined as the contrast of a point source whose peak pixel is equal to the background.

At λ = 4.6 μm, coronagraphic PSF subtraction can reduce the already-suppressed wings by an additional factor of 30 – 100 when the wavefront difference between the two PSFs is <10 nm RMS (a net total reduction factor of 51 – 430). As the difference increases, so do the subtraction residuals. At 40 nm RMS, at the most pessimistic limit for instability, the improvement from subtraction is only a factor of 10 – 30. At shorter wavelengths, where the effects of wavefront errors are greater, subtractions will also be less effective.

In actual observations, the detection limit is set by the flux of the planet relative to the local background noise as measured either in an aperture or with a matched filter (i.e. PSF fitting). In PSF-subtracted images the total noise is a combination of read noise in the target and reference star images, shot noise from the wings of the PSF and sky background in each image, subtraction residuals caused by PSF mismatches, and shot noise from planet itself. Increasing the total exposure time will reduce the shot and read noise relative to the planet flux, but it will not affect the ratio of the planet flux to the PSF subtraction residuals. The primary advantage of the NIRCam coronagraph over direct imaging is not the immediate reduction in the brightness of the PSF wings but rather the reduced sensitivity to PSF mismatches that result in subtraction residuals.

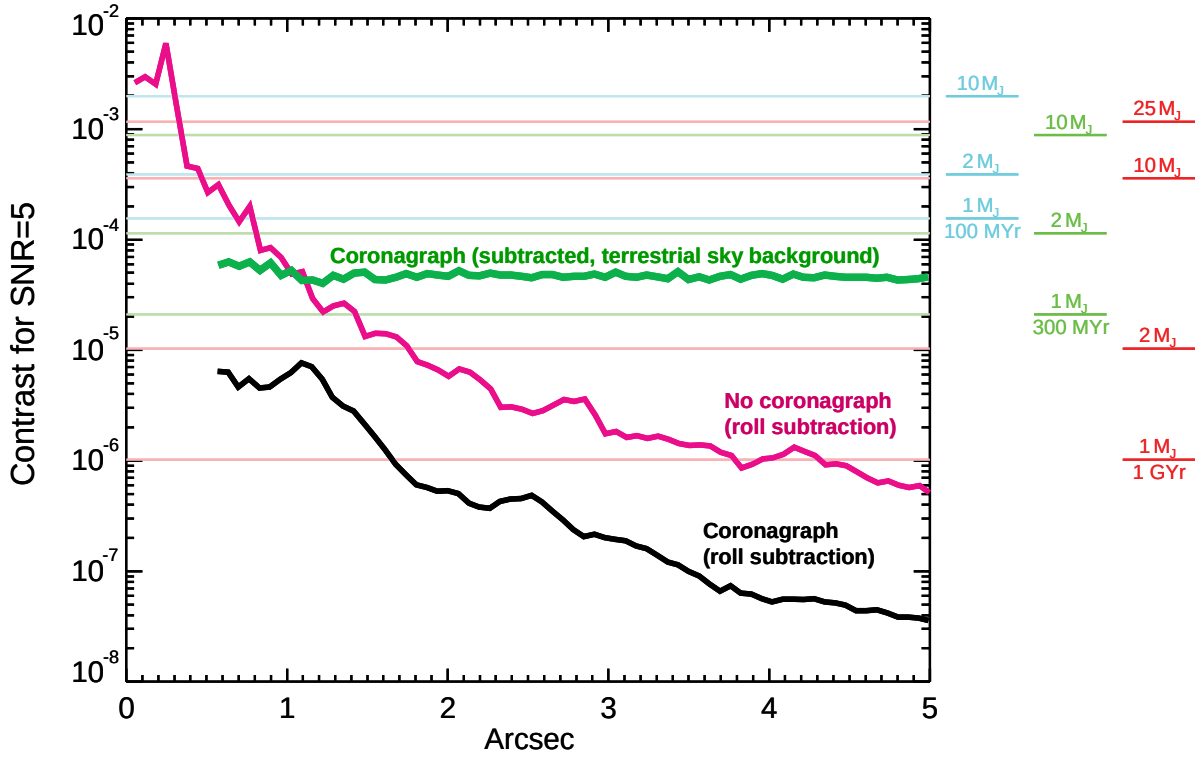

Figure 9. Mean azimuthal contrast at which a signal-to-noise ratio of 5 detection of a planet around an M0V star at 4 pc is obtained in filter F460M with the wedge occulter (wedge region excluded). The corresponding planet masses and ages are shown on the right. The profiles are derived from roll-subtracted model images (20 nm RMS wavefront difference between rolls in addition to static aberrations) for both non-coronagraphic and coronagraphic observations. At each orientation, a 10000 sec exposure was obtained. Detector and zodiacal background noise is included. The thick green line shows the contrast of the same coronagraph (roll subtraction) with the sky background seen at Mauna Kea.

7. SCIENCE WITH THE NIRCAM CORONAGRAPH

7.1 Extrasolar planets

The most exciting science expected from the NIRCam coronagraph is the detection of planets around other stars. NIRCam can take advantage of the peak in thermal emission at $\lambda = 4.6$ μm where a large planet is magnitudes brighter relative to the star than it is at other wavelengths. As shown in Figures 2 and 8, observations in different NIRCam filters can be used to distinguish planets from other objects such as background stars that would have more uniform flux distributions.

Because it is seen in emitted rather than reflected light at these wavelengths, a planet's brightness is not dependent on its distance from or the luminosity of the star at the observable separations. The NIRCam coronagraph will enable imaging of planets with masses <1 M_{Jup} and ages of up to a few billion years around nearby, low-luminosity stars. As shown in Figure 9, a 1 Gyr-old Jupiter would have a contrast of 10^{-6} relative to an M0V star. As the star's luminosity increases, the planet's contrast decreases, so planet searches will likely concentrate on K, M, and L stars. Nearby associations of young

(~20-50 Myr) stars, such as the Beta Pictoris moving group, will also be candidates for searches, though because of their greater distances (>20 pc), any detectable planets will be further out than Jupiter's orbit (5 AU).

An example of the potential number of planets that the NIRCam coronagraph may find is provided in Table 1. A Monte Carlo analysis was done to determine planet detectability around 49 actual stars of types M5 or earlier within 6 parsecs. The stars were assigned random ages of 0.1 – 5 Gyrs. The detection limit was set to a signal-to-noise ratio (SNR) of 10 with roll subtraction and one hour exposures per roll in F460M and 20 nm RMS of wavefront difference between rolls. A planet twice the mass of Jupiter and at the same orbital radius would be seen around nearly half of the stars. The results would be even more favorable if later type M and L stars were included.

Table 1. Number of stars of type M5 and earlier around which planets would be detectable (SNR=10) with the NIRCam coronagraph. Based on a Monte Carlo analysis of 49 nearby stars with ages of 0.1 – 5 Gyrs.

Projected Distance from Star (AU)	Planet Mass (M_{Jup})		
	1	2	10
1	0	1	1
3	3	15	26
5	6	24	47
7	7	27	47
10	8	33	48
15	9	39	48
20	9	43	48
25	9	44	48

7.2 Circumstellar disks

Circumstellar dust disks are the most visible signs of the planet formation process. The protoplanetary disks around young (<1 Myr) stars are optically-thick and rich in gas which accretes onto the star during the time that massive planets are expected to coalesce. Many such disks have been resolved using ground-based telescopes and the Hubble Space Telescope. They are relatively easy to image when viewed edge-on, as the dense disks block the direct light from the stars. When viewed from any other inclination, however, the glare from the stars can overwhelm the much fainter disks. After these disks have been accreted onto the star or have condensed into planetoids (comets, asteroids) and planets, they evolve into more tenuous, less massive, dusty disks filled with the debris from the collisions of these bodies, such as the famous disk around Beta Pictoris. These optically thin disks are difficult to see under any circumstance, as the total amount of reflected light of even the brightest debris disk is much less than 1% of the stellar flux. Thus, for both types of disks a coronagraph is needed.

Protoplanetary and debris disks have been resolved over a wide range of wavelengths, but not over the 2 – 5 μm range where NIRCam can make unique contributions. At these wavelengths, the disks will be seen in scattered light with the coronagraph, and these new observations will provide new constraints on dust grain properties. Structural details in the disks (Figure 10) will seen best at shorter wavelengths, about 2 μm, where the resolution is better. Wavefront errors and chromatic dispersion from the Lyot stop wedge will probably limit the ability to observe at shorter wavelengths. The wavefront stability of JWST will be a primary limiting factor.

We note that the ultimate contrast achieved with the NIRCam coronagraph will be about 10× worse than the coronagraphs on the Hubble Space Telescope (notably, the ACS coronagraph), due to the complexity and aberrations in the JWST PSF. Therefore, it is unlikely that JWST will be used extensively to search for previously unseen debris disks in scattered light, as most of the candidate targets have already been observed with HST at better contrast levels. In non-thermal emission imaging, JWST's primary contribution will be characterization of known debris disks at previously unobtainable wavelengths and discovering new protoplanetary disks and perhaps stellar jets near young stars.

8. ACKNOWLEDGEMENTS

This work was undertaken at the NASA Jet Propulsion Laboratory with support provided by the NIRCam instrument development team (NASA NAS5-02105). Marc Kuchner provided suggestions for potential band-limited occulter profiles.

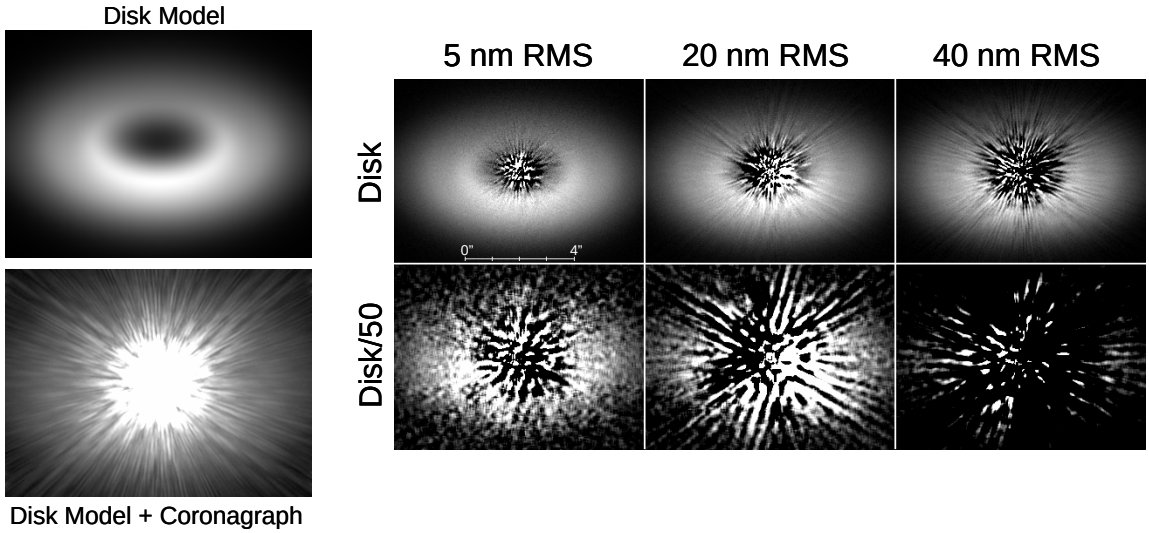

Figure 10. Simulated scattered-light images of a circumstellar dust disk based on a simplified model of the HD 141569A disk[8]. The images are 9" wide. The disk has a 8×10^{-3} fractional infrared luminosity (3× more than Beta Pictoris). The simulated disk model without the star is shown in the top left, and below it is the disk and star (A0V at 100 pc) observed with the NIRCam coronagraph in F200W using the 0.4" spot occulter, prior to PSF subtraction. The panel on the right shows images of the simulated disk after subtraction of a similarly exposed image of an A1V reference star. The differences between the target and reference image wavefront errors are indicated (in addition to a ~131 nm static wavefront error prior to the occulter). The bottom row shows the same disk if it had 1/50 the optical depth (1.6×10^{-4} fractional IR luminosity), and those images have been smoothed by a 5 x 5 pixel boxcar. The observations include noise and represent a 5000 sec exposure time.

REFERENCES

1. J. T. Trauger and W. A. Traub, "A laboratory demonstration of the capability to image an Earth-like extrasolar planet," *Nature*, **445**, 771 (2007).
2. A. Burrows, D. Sudarsky, and J. I. Lunine, "Beyond the T Dwarfs: Theoretical Spectra, Colors, and Detectability of the Coolest Brown Dwarfs," *Astrophysical Journal*, **596**, 587 (2003).
3. P. A. Lightsey, A. A. Barto, and J. Contreras, "Optical Performance for the James Webb Space Telescope," in *Proc. of the SPIE*, **5487**, 825 (2004).
4. M. J. Kuchner and W. A. Traub, "A Coronagraph with a Band-limited Mask for Finding Terrestrial Planets," *Astrophysical Journal*, **570**, 900 (2002).
5. A. Boccaletti, P. Baudoz, J. Baudrand, J. M. Reess, and D. Rouan, "Imaging exoplanets with the coronagraph of JWST/MIRI," *Advances in Space Research*, **36**, 1099 (2005).
6. J. J. Green, C. Beichman, S. A. Basinger, S. Horner, M. Meyer, D. C. Redding, M. Rieke, and J. T. Trauger, "High Contrast Imaging with the JWST NIRCam Coronagraph," in *Proc. of the SPIE*, **5905**, 185 (2005).
7. J. E. Krist, "PROPER: An Optical Propagation Library for IDL," in *Proc. of the SPIE*, **6675** (2007).
8. M. Clampin, et al. "Hubble Space Telescope ACS Coronagraphic Imaging of the Circumstellar Disk around HD 141569A," *Astronomical Journal*, **126**, 385 (2003).